POLITECNICO DI TORINO
Repository ISTITUZIONALE

Assessing the retrofitability of direct-injection hydrogen technology for off-road engines: Numerical and experimental investigations

Original
Assessing the retrofitability of direct-injection hydrogen technology for off-road engines: Numerical and experimental investigations / Scalambro, A., Piano, A., Millo, F., Scinicariello, N., Lodi, W., Mallamo, F., Loiodice, R., Jagodzinski, B., Dhongde, A.. - In: FUEL PROCESSING TECHNOLOGY. - ISSN 0378-3820. - 289:(2026). [10.1016/j.fuproc.2026.108477]

Availability:
This version is available at: 11583/3010788 since: 2026-05-13T07:49:00Z

Publisher:
Elsevier

Published
DOI:10.1016/j.fuproc.2026.108477

Terms of use:

This article is made available under terms and conditions as specified in the corresponding bibliographic description in the repository

Publisher copyright

(Article begins on next page)

11 November 2026

Fuel Processing Technology 289 (2026) 108477

Contents lists available at ScienceDirect

Fuel Processing Technology

journal homepage: www.elsevier.com/locate/fuproc

Assessing the retrofitability of direct-injection hydrogen technology for off-road engines: Numerical and experimental investigations

Andrea Scalambro [a], Andrea Piano [a,*], Federico Millo [a], Nicola Scinicariello [b], Wladimir Lodi [b], Fabio Mallamo [c], Rosario Loiodice [c], Bartosch Jagodzinski [d], Avnish Dhongde [d]

[a] Politecnico di Torino, Corso Duca degli Abruzzi, 24, Torino (IT)
[b] Rehlko, Via Cavaliere del Lavoro Adelmo Lombardini, 2, Reggio Emilia (IT)
[c] FEV Italy, Via Livorno, 60, Torino (IT)
[d] FEV Europe Gmbh, Neuenhofstraße, 181, Aachen (DE)

ARTICLE INFO

Keywords:
Hydrogen direct-injection engine
Alternative fuels
3D-CFD
Hydrogen engine calibration
Retrofitability

ABSTRACT

Hydrogen-powered internal combustion engines offer a viable pathway toward low-carbon propulsion while leveraging existing engine architectures. This study presents the conversion of a state-of-the-art 2.4 L diesel engine for off-road applications to direct-injection hydrogen operation through an integrated numerical-experimental approach. Three-dimensional CFD simulations were employed to optimize hydrogen injection and mixture formation, with the scope of reducing mixture stratification, while requiring only minor design modifications (Φ_σ/Φ_{Avg} from values greater than 45% to approximately 15–25%). Based on these results, a prototype engine was developed and experimentally tested. The hydrogen engine achieved performance comparable to the baseline diesel unit, reaching 305 Nm and 55 kW with peak indicated thermal efficiency above 40%. Over the LSI-NRTC homologation cycle, engine-out NO_x emissions reached 0.68 g/kWh, well below EU Stage V and EPA Tier 5 limits. With the integration of an SCR system, tailpipe NO_x emissions were further reduced to 0.03 g/kWh, approaching near-zero levels, with only a limited torque derating (< 5%).

1. Introduction

Anthropogenic emissions of greenhouse gases are widely recognized as the primary drivers of climate change [1–3]. At a global level, the transport sector – including road, aviation, and shipping – accounted for 22% of the total carbon dioxide (CO2) emissions in 2023 [4]. This significant contribution has driven policymakers and legislators to enforce stringent regulations for an expedited transition of the transport sector toward decarbonized solutions [5,6]. Powertrain manufacturers are addressing this technological shift through a wide range of solutions, tailored to meet the specific needs of different applications and market segments [7,8]. In the passenger car and light-duty vehicle sectors, hybrid electric vehicles offer a valuable short- to mid-term solution for decarbonization. Although battery electric vehicles (BEVs) are gaining a larger market share [9], their widespread adoption is currently constrained by technical factors such as long recharging times and limited driving range. Additionally, the carbon footprint of BEVs, when assessed on a life-cycle-analysis basis, is significantly influenced by the energy mix of the electrical grid [10,11]. For heavy-duty (HD) applications, the operational demands and the requirement for bulk battery packs make

Abbreviations: AMR, Adaptive Mesh Refinement; BEV, Battery Electric Vehicle; BMEP, Brake Mean Effective Pressure; COV, Coefficient of Variation; MFB50, Combustion Anchor Angle; MFB1090, Combustion Duration; CR, Compression Ratio; CFD, Computational Fluid Dynamics; CFL, Courant Friedrich Lewy; CAD, Crank Angle Degree; DI, Direct Injection; EOI, End of Injection; EM, Engine Map; EATS, Exhaust After Treatment System; FS, Full Scale; HD, Heavy-Duty; HPDI, High-Pressure Direct Injection; IMEP, Indicated Mean Effective Pressure; ITE, Indicated Thermal Efficiency; ICE, Internal Combustion Engine; LSI, Large Spark Ignition; LET, Low-End Torque; LP, Low Pressure; NRTC, Nonroad Transient Cycle; OEM, Original Equipment Manufacturer; PFP, Peak Firing Pressure; PFI, Port Fuel Injection; λ, Relative Air-to-Fuel Ratio; RNG, Renormalization Group; RANS, Reynolds-Averaged Navier-Stokes; SCR, Selective Catalytic Reduction; SOI, Start of Injection; TDC, Top Dead Centre; VNT, Variable Nozzle Turbine; WP, Working Point.

* Corresponding author.
E-mail addresses: andrea.scalambro@polito.it (A. Scalambro), andrea.piano@polito.it (A. Piano), federico.millo@polito.it (F. Millo), nicola.scinicariello@kohler.com (N. Scinicariello), wladimir.lodi@kohler.com (W. Lodi), mallamo@fev.com (F. Mallamo), loiodice@fev.com (R. Loiodice), jagodzinski@fev.com (B. Jagodzinski), dhongde_a@fev.com (A. Dhongde).

https://doi.org/10.1016/j.fuproc.2026.108477
Received 20 March 2026; Received in revised form 17 April 2026; Accepted 3 May 2026
0378-3820/© 2026 The Authors. Published by Elsevier B.V. This is an open access article under the CC BY license (http://creativecommons.org/licenses/by/4.0/).

this powertrain configuration impractical [12]. In off-road and agricultural applications, BEVs do not appear to be particularly suitable because minimizing operational costs and maximizing machine productivity require short refuelling time. Additionally, the necessity of operating the machine near an electric grid would reduce operational flexibility in these contexts. Compared to BEVs, hydrogen-based systems address issues related to range and refuelling time and offer advantages in terms of powertrain space and weight thanks to the higher energy density of hydrogen. Besides this, hydrogen serves as both an energy carrier and an energy vector, thus supporting and enhancing the transition toward a sustainable and decarbonized economy [13]. Fuel cell electric vehicles (EVs) feature relatively high efficiency, especially at part-mid loads [14]. However, in certain applications, such as off-road vehicles, the dusty operating environment, and critical ambient conditions present significant challenges for the health of fuel cell stacks and their thermal management [15].

In this context, hydrogen internal combustion engines (H_2-ICEs) may bridge this gap, offering a reliable and robust solution for carbon-neutral operation at affordable costs for development, integration in existing machines, production, and maintenance. Indeed, H_2-ICEs can be directly derived from commercially available engines, avoiding the need to completely design a powertrain from scratch, thus limiting development resources. Additionally, compared to fuel cell applications, H_2-ICEs may benefit from mature manufacturing processes and facilities along with a well-established supply chain [16]. Moreover, the carry-over of several powertrain components greatly simplifies integration into existing vehicles, further reducing adaptation requirements. Lastly, hydrogen has excellent combustion properties, such as a high laminar flame speed over a wide range of pressure, temperature, relative air-to-fuel ratios (λ), and residuals concentration, a high lean flammability limit, a large lower heating value (i.e., 120 MJ/kg) [17]. However, the minimum ignition energy of hydrogen is roughly one order of magnitude lower than that of conventional fossil fuels (i.e., 0.016 mJ) [18]. This strongly increases the risk of preignition [19,20], glow ignition [21,22], and backfiring [23,24], in the case of external mixture preparation.

High-pressure direct injection (HPDI) systems, enabling a diffusive combustion process of hydrogen allow for avoiding the mentioned risks as well as those related to abnormal combustion processes (e.g., preignition and knock). Moreover, hydrogen HPDI fuel systems can achieve efficiency levels up to 51% and loads up to 30 bar of brake mean effective pressure (BMEP) [25,26]. Nevertheless, the integration of a high-pressure injector into the cylinder head and the increased system complexity required to increase hydrogen pressure up to 300 bar, make this solution practical only for HD applications. Moreover, the high nitrogen oxides (NO_x) emissions associated with a diffusive combustion process makes mandatory the adoption of a dedicated aftertreatment system [27]. On the other hand, combustion systems based on the conventional spark ignition (SI) cycle (Otto cycle) can provide acceptable efficiency levels (up to 44% [25]) while significantly reducing complexity. Low pressure (LP) port fuel injection (PFI) systems, characterized by an injection pressure between 5 and 10 bar represent the straightforward approach for retrofitting an existing engine. Indeed, it does not lead to integration issues, and it can rely on injection systems with low failure risk. Moreover, knock tendency and NO_x emissions are strongly reduced [28] and combustion variability is minimized [29] thanks to the high level of in-cylinder mixture uniformity. Nonetheless, injection timing and valve phasing must be carefully optimized in order to limit safety problems related to backfire [30]. Moreover, the selection of the boosting system poses a significant challenge. Indeed, in H_2-ICEs, the high air excess needed to reduce the risk of abnormal combustion phenomena and hinder the formation of NO_x [31] significantly increases air requirements [32]. In PFI systems, the injection of hydrogen in the intake ports further reduces the volume of intake air, generally resulting in lower power output and lower efficiency [33]. Lastly, as the average λ is increased, the temperature of the exhaust gases is reduced, lowering the available exhaust enthalpy and severely limiting boosting performances [34–36]. The performances of PFI H_2-ICEs, in terms of maximum load, combustion stability, and NO_x emissions, can be improved by equipping the engine with an active pre-chamber. In [37], the adoption of an active pre-chamber system on an HD engine for off-road applications, enabling turbulent jet ignition (TJI) operation, allowed to achieve the same performances as the original diesel engine, with engine-out NO_x emissions (0.24 g/kWh) below the current legislated tailpipe limit of 0.4 g/kWh over the Non-Road Transient Cycle (NRTC). However, this combustion system requires the adaptation of the cylinder head to fit the pre-chamber and the installation of one additional injector per cylinder, thus increasing the number of design modifications.

In contrast, LP direct injection (DI) systems can address many of the limitations of PFI H_2-ICEs, either partially or completely, without significantly increasing hardware complexity. Indeed, backfiring is avoided thanks to the injection of hydrogen directly inside the combustion chamber. For the same reason, boosting demand is significantly reduced compared to a PFI H_2-ICE. In [38] it was demonstrated that the intake manifold pressure in a DI single-cylinder engine with a displacement of 2.13 l is reduced by 200 mbar compared to the PFI system at the same excess air ratio. DI systems also enhance transient performance. As a matter of fact, they can exploit post-injection strategies to increase the enthalpy of exhaust gases, thereby improving dynamic operations [39–41]. However, in DI H_2-ICEs, mixture inhomogeneities might lead to higher NO_x emissions [38] and increase the likelihood of knock [42] and pre-ignition [43]. Therefore, the optimization of the air-hydrogen mixing process is a crucial factor for suppressing abnormal combustion processes and reducing engine-out emissions. Advanced injection timings generally lead to higher uniformity levels [44], and lower NO_x emissions. Nonetheless, if the injection occurs too early during the intake process, some hydrogen can flow back into the intake ports [45], potentially leading to backfire. Moreover, volumetric efficiency decreases, while compression work is increased [46], partially reducing the benefits of a DI layout. On the other hand, excessively late injection timings generally reduce mixture uniformity, increasing combustion variability and NO_x formation [47]. Nevertheless, a suitable optimization of the injection timing, hydrogen targeting, and interaction with the in-cylinder aerodynamics can strongly enhance fast and effective air-hydrogen mixing [48–56]. The effectiveness of such a technology has already been extensively demonstrated by several works in the literature [11,20,40,52,57–62], most of which either are for HD applications [40,52,62] or are based on a design from scratch [11,44]. However, very little is currently known about the performances of relatively low-displacement DI H_2-ICE for off-road applications.

In this context, the present study aims to evaluate the possibility of developing a DI H_2-ICE from a diesel engine for off-road applications through limited modifications, while achieving equivalent performance. This approach allows original equipment manufacturers (OEMs) to limit investments, shorten development time, and significantly simplify the installation of carbon-free solutions into existing machinery and vehicles. Consequently, this approach largely preserves the existing supply chain and production facilities, thereby facilitating market penetration. The technical targets of the project can be summarized as follows:

1. High retrofitability potential and low conversion costs
2. Same performance as the base diesel engine. Maximum torque of 305 Nm @ 1500 rpm and rated power of 55 kW @ 1800 rpm - 2600 rpm
3. Peak indicated thermal efficiency (ITE) above 40%
4. Engine-out NO_x emissions below Stage V limits (4.70 g/kWh of NO_x and non-methane hydrocarbons) over the NRTC
5. Near zero tailpipe NO_x emissions with exhaust after treatment systems (EATS)

To address these challenging tasks, a three-dimensional Computational Fluid Dynamics (3D-CFD) methodology, validated against

experimental data gathered from a low-pressure chamber, was first developed and employed to analyse and optimize the injection and mixture formation processes. Based on the outcomes of the numerical analysis, an engine prototype was subsequently built and tested on the dynamic test bench. The paper is organized as follows. First, the case study is introduced, highlighting the main specifications of the baseline diesel engine and the key design modifications implemented to enable hydrogen operation. Then, the analysis of the injection and air–hydrogen mixing process, carried out through 3D-CFD simulations, is presented. Finally, the engine sensitivity to the main calibration parameters is analysed, followed by the discussion of experimental engine maps and performance results under the NRTC cycle.

2. Test case

A state-of-the-art 2.4-l, four-cylinder in-line engine, designed for diesel operation in off-road applications and compliant with TIER 4 Final/STAGE III B regulations, was selected as the reference case. It can achieve a maximum torque of 305 Nm at 1500 rpm and a rated power of 55.4 kW at 2600 rpm. It is equipped with a high-pressure (2000 bar) common rail injection system and a wastegate turbocharger with an aftercooler. The cylinder head is flat, featuring 4 valves per cylinder with fixed actuation, a central injector, and a lateral glow plug. Lastly, the helical shape of the intake ports provides a quite intense swirl motion to the charge admitted into the cylinder. More details on the geometrical features of the combustion chamber are reported in Table 1.

To enable hydrogen operation, a reduction in the compression ratio is necessary. In LP-DI H_2-ICEs, defining the compression ratio significantly impacts the trade-off among performance, efficiency, and emissions. Although a high CR can lead to greater thermal efficiency, it also results in higher NO_x emissions and increases the likelihood of knocking. Consequently, a delayed combustion process would be required to mitigate these issues, which would in turn deteriorate efficiency. In light of this, the CR was conservatively reduced from 17:1 to 11:1 for the first engine generation. The reduction in the compression ratio was achieved by increasing the volume of the piston bowl and slightly shortening the length of the connecting rod. To avoid altering the cylinder head design, the LP hydrogen injector was mounted laterally and near the cylinder liner in place of the glow plug, while the spark plug replaced the central diesel injector. Moreover, the sealing angle of both the intake and exhaust valves was reduced from 45° to 30° to limit their wear. All other components were carried over from the base diesel engine. Finally, a forced crankcase ventilation system was designed to maintain the hydrogen concentration within the crankcase below 2%, thereby avoiding the risk of uncontrolled combustion processes.

3. Simulation tool chain

As widely recognized, numerical simulations represent a powerful tool to speed up and support the engine design process, as they significantly reduce the need for costly and time-consuming experimental campaigns. A well-established 1D/3D-CFD synergistic methodology was adopted to investigate the gas exchange process and optimize the mixture formation process, respectively. Specifically, mono-dimensional simulations were employed to define the most suitable boosting solution, both in terms of layout and turbine and compressor sizing and to optimize exhaust and intake valve timing and lift. Meanwhile, multi-dimensional simulations provided detailed insights into the hydrogen-air mixing process, enabling further refinement and ultimately improving mixture uniformity. For reasons of clarity and conciseness, the complete 1D-CFD analysis has been omitted.

3.1. 3D-CFD analysis

In DI H_2-ICE, the optimization of the mixture formation process is crucial for enhancing combustion stability, reducing NO_x emissions, and minimizing the risk of abnormal combustion events. Indeed, while in PFI engines the high degree of mixture uniformity leads to almost zero NO_x emissions under ultra-lean operations [28,33], NO_x formation in DI H_2-ICEs can increase significantly, particularly when dealing with highly inhomogeneous and stratified mixtures [53]. Moreover, combustion variability can drastically increase if lean pockets are located in the vicinity of the spark plug when combustion is triggered, whereas the presence of a rich mixture in the end-gases can promote the onset of knock. In this context, 3D-CFD Reynolds-Averaged Navier-Stokes (RANS) simulations were exploited to study and analyse the injection and hydrogen-air mixing processes with the aim of maximizing mixture uniformity. Numerical simulations were performed in the rated power working point (Table 2). This WP was selected for the analysis because achieving a high degree of mixture homogeneity is particularly challenging due to the long injection duration and the limited available mixing time.

3.1.1. Numerical model setup

Multidimensional numerical simulations were carried out by means of Converge CFD v3.0 adopting a RANS approach. Time-dependent boundary conditions, in terms of temperature, pressure, and species concentrations were derived from a 1D-CFD GT-SUITE complete engine model along with all the data required to properly initialize the computational domain. As shown in Fig. 1, the computational domain was discretized using an orthogonal mesh with a base cell size of 2.0 mm. Local mesh refinements were applied within the cylinder, particularly near the intake and exhaust valves (down to 0.50 mm and 1.00 mm, respectively), to accurately capture the main in-cylinder flow structures generated during the gas exchange process. A minimum grid size of 0.25 mm was achieved in the region downstream of the injector, in line with previous numerical studies on similar engine configurations [63]. The Adaptive Mesh Refinement (AMR) algorithm was employed to dynamically refine the grid (down to 0.25 mm) based on sub-grid scale gradients of temperature, velocity, and hydrogen concentration. Additionally, near-wall regions were refined through AMR to ensure adequate resolution compatible with the adopted wall-function approach. This aspect is particularly important for hydrogen-fuelled applications, where accurate prediction of near-wall gradients significantly affects species diffusion and overall combustion behaviour.

Turbulence modelling heavily affects the simulation of the hydrogen-air mixing process. In [64], it was shown that all $k-\varepsilon$ turbulence models (i.e., standard $k-\varepsilon$, realizable $k-\varepsilon$ and $k-\varepsilon$ with renormalization group (RNG)) provide similar predictions for jet penetration and hydrogen dispersion in the cylinder. Among these, the RNG $k-\varepsilon$ turbulence model was selected for the present work due to its effectiveness

Table 1
Combustion chamber technical specifications.

Displacement [l/cyl.]	0.62
Bore [mm]	88
Stroke [mm]	102
Compression Ratio (CR) [−]	17:1 (Diesel ICE) 11:1 (H_2-ICE)
Number of valves [−]	4
Air motion [−]	Swirl

Table 2
Working point selected for the 3D-CFD analysis.

Speed [rpm]	2600
BMEP [bar]	10.3
λ [−]	2.3
p_{boost} [bar]	2.24
$T_{Int.Man.}$ [K]	332

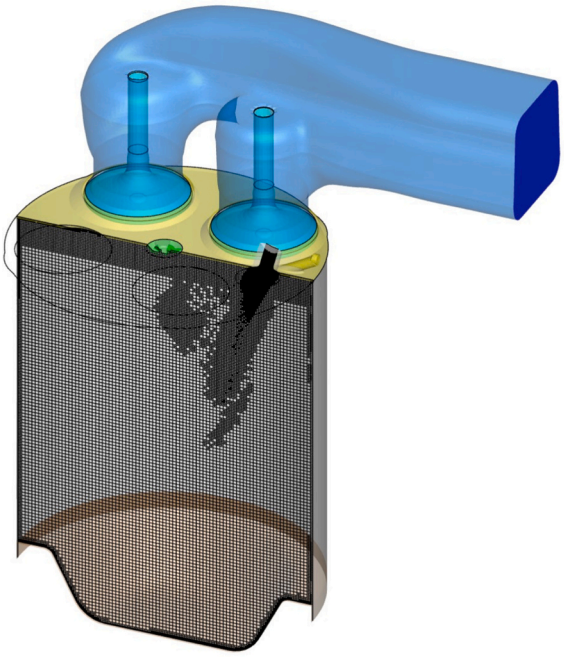


Fig. 1. Combustion system geometry and mesh topology at 180 CAD before TDC of firing.

in accurately capturing the evolution of rotating structures [65,66], such as swirl and tumble. Even though the decrease of the turbulent Schmidt number has proven to reduce the discrepancy between experimental data and simulation results [64], the default value ($Sc = 0.78$) was used in this study due to the lack of experiments. This approach ensures that the worst-case scenario is considered throughout the simulation activity. Kinetic and thermal boundary layers were modelled through the law of walls, and the O'Rourke and Amsden model [67] was selected to describe the heat transfer. As far as the simulation of the injection process is concerned a dedicated methodology has been adopted. Specifically, the bottom portion of the LP hydrogen injector was included in the fluid domain. Both the injection pressure and the actual injector valve profile were imposed, thus the hydrogen mass flow rate was directly computed by the software and compared to the experimental data, provided by the injector supplier. Lastly, a variable time-step algorithm was used to limit the simulation time-step based on the Courant Friedrich Lewy (CFL) numbers ($CFL_{Convection} = 1.0$, $CFL_{Diffusion} = 2.0$, and $CFL_{Mach} = 50.0$). The described numerical model has been extensively validated through comparison with experimental data obtained from an optically accessible chamber across various injection pressures, ambient pressures, and injection durations [68,69]. More details on the numerical schemes employed can be found in [70].

3.1.2. *Mixture formation process – Optimization results*

The present study aims at developing a DI H_2-ICE through only minor and strictly necessary modifications to the original diesel engine architecture. In this context, major design interventions. Such as redesigning the intake port geometry (e.g. to promote tumble motion [62]), modifying the cylinder head to accommodate the LP H_2 injector with optimized position and inclination, or enhancing the cooling jacket, were intentionally not considered. Instead, the focus was placed on limited modifications that can be implemented without altering the core engine design, such as adjustments achievable through final machining operations. Consequently, most of the 3D-CFD analyses focused on operating parameters (i.e., injection timing) and geometrical features (i.e., jet cap design and intake valve seat geometry) that can be implemented on the base engine with minimal design efforts.

The start of injection (SOI) was set to coincide with the intake valve closure in order to prevent hydrogen backflow into the intake ports, while ensuring sufficiently long mixing time [70]. Afterwards, an optimization study was carried out on the jet cap geometry. When properly designed, jet caps can significantly enhance mixture uniformity [48–51,71,72]. Several injector jet caps, both single- and multi-hole, were designed and tested. In the present work, results are reported only for two of them, and both were compared with the no-cap design. These are:

- Central cap: single-hole configuration oriented toward the centre of the combustion chamber. It was designed to enhance the hydrogen-air mixing process by exploiting more intense air entrainment.
- Liner cap: single-hole configuration oriented toward the cylinder liner (corresponding to a 180° rotation of the central cap about the injector axis). This design aims to promote hydrogen–air mixing by inducing a strong tumble motion, effectively exploiting the interaction between the high-velocity hydrogen jet and the piston bowl.

Fig. 2 shows isosurfaces of hydrogen mass fraction at 1%, used to identify the outer boundary of the hydrogen plume, together with velocity field distributions on a plane passing through the injector axis.

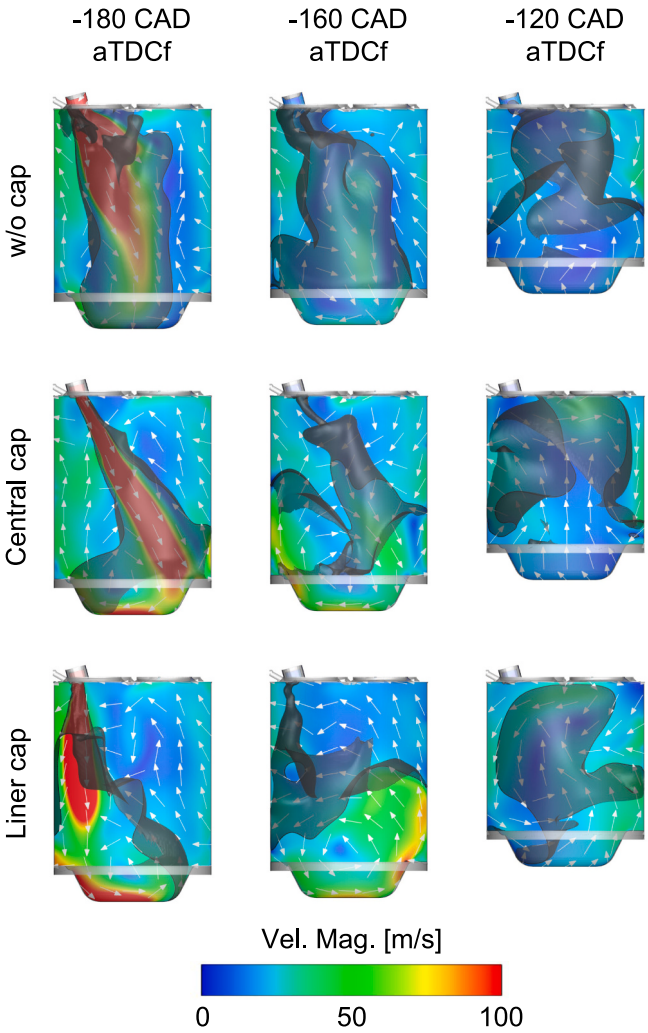


Fig. 2. Iso-surfaces of hydrogen mass fraction at 1% and velocity field distribution on a plane passing through the injector axis at − 180, − 160, and − 120 CAD aTDCf for the configurations without jet cap (top), with Central cap (middle), and with Liner cap (bottom).

These are reported at − 180, − 160, and − 120 crank angle degrees (CAD) aTDCf to highlight the impact of the injection event on the main in-cylinder flow structures. In the baseline configuration, which does not include any jet cap (top row), the injected hydrogen splits into two distinct flow paths due to the Coanda effect. One portion adheres to the flame deck, while the remainder advances along the injector axis. Shortly after the end of injection (− 160 CAD aTDCf), the jet structure becomes strongly distorted by the in-cylinder swirl, causing the bulk of the hydrogen to move toward the bowl centre. When adopting the *central cap* configuration (middle row), the hydrogen jet is efficiently redirected toward the chamber centre, preventing attachment to the flame deck. The jet preserves a compact and coherent shape rather than splitting into separate streams, as observed in the reference case. After impinging on the piston bowl wall (− 180 and − 160 CAD aTDCf), the jet deflects generating a pronounced tumble flow. A similar effect is achieved by the *liner cap*, although in this configuration the jet penetrates more vertically into the combustion chamber and interacts with the opposite side of the piston bowl compared to the *central cap*. As a result, the induced tumble vortex develops with an opposite rotational direction relative to that generated by the *central cap*.

To assess the degree of mixture homogeneity, the relative standard deviation (σ_{Rel}) was adopted, defined as the ratio between the standard deviation (Φ_σ) and the mean value of the equivalence ratio (Φ_{Avg}). In contrast to the commonly used uniformity index (UI), lower σ_{Rel} values indicate a more uniform mixture. Fig. 3 reports the hydrogen distribution at the TDCf for the three configurations together with σ_{Rel} and the corresponding mass fraction classified by λ. From a global viewpoint, the enhanced interaction between the hydrogen jet and the piston bowl, obtained through optimized jet targeting, markedly improves the overall mixing performance. Although the strong swirl generated by the helical intake ports tends to create a non-uniform, circular-arc-shaped λ distribution (top view in Fig. 3), the strengthened jet-piston interaction mitigates vertical stratification (front view in Fig. 3), leading to a more homogeneous charge. Among the tested designs, the *central cap* provided the best mixing performance. At TDCf, σ_{Rel} decreases from over 45% (capless) to slightly below 30%. As indicated by the histograms in the lower section of Fig. 3, the share of ultra-lean mixture ($\lambda > 3$) drops from approximately 31% to less than 18%, while the portion within optimal λ levels ($2.0 < \lambda < 2.6$, i.e., average $\lambda \pm 0.3$) increases from 23% to 34%. Simultaneously, the rich region ($\lambda < 1.5$) shrinks from 18% to below 5%. The *liner cap* achieves an intermediate uniformity ($\sigma_{Rel} = 34.6\%$ at TDCf). In this case, the strong jet-induced tumble weakens during the compression stroke, allowing the swirl motion to dominate and drive hydrogen rotation around the cylinder axis, ultimately confining the mixture near the liner and reducing air utilization. Consequently, over 25% of the in-cylinder charge falls within the ultra-lean region ($\lambda > 3$), while approximately 17% lies below $\lambda = 1.5$.

Finally, after having identified the optimal jet-cap configuration, the influence of swirl intensity on mixture formation was investigated. Variations in swirl were achieved by modifying the intake valve seat geometry. This approach was selected to preserve the original cylinder head architecture of the diesel engine, thus minimizing hardware changes during conversion to hydrogen operation. Three chamfer configurations were developed and evaluated through numerical simulations (Fig. 4):

- Swirl chamfer on the long port (baseline): corresponding to the current diesel setup, in which the long-port chamfer is machined eccentrically to reinforce the swirl generated by the helical intake ports.
- No swirl chamfer: both chamfers are concentric, resulting in a swirl motion entirely driven by the intake port geometry.
- Counter-swirl chamfer on the long port: the long-port chamfer is eccentrically shaped to induce a swirl direction opposite to

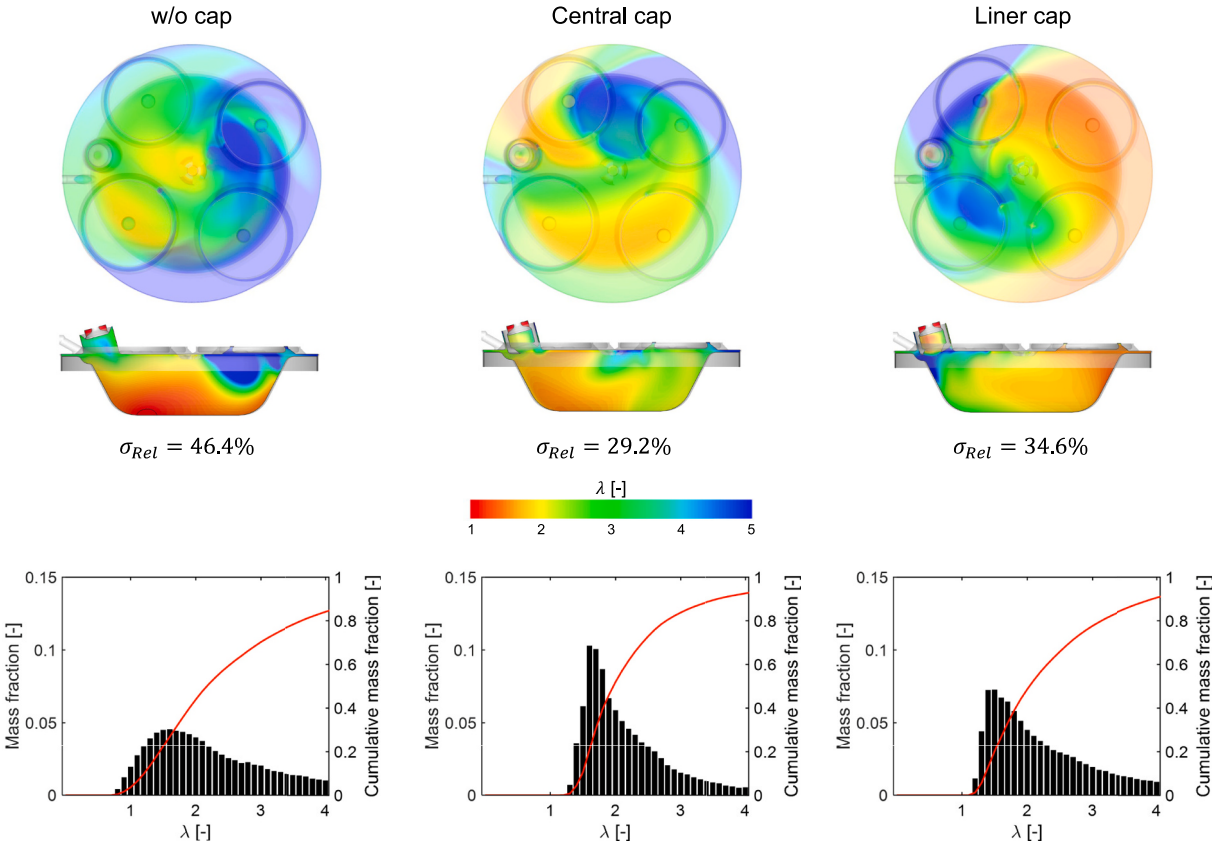


Fig. 3. λ distribution at TDC of combustion (top) and cylinder mass distribution on a λ basis (bottom) for the configurations without jet cap (left), and with central (middle) and liner cap (right).

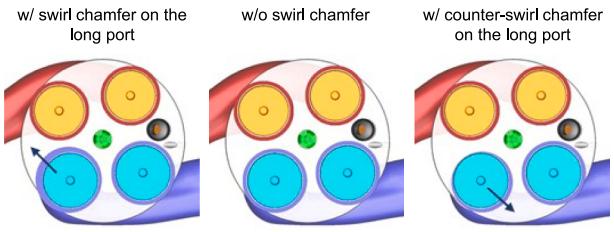


Fig. 4. Bottom view of the flame deck for the three swirl chamfer configurations, with the intake valve seat eccentricity highlighted.

that produced by the intake ports, while the short-port chamfer remains concentric. This configuration effectively neutralizes the global in-cylinder swirl.

The simulations were conducted using the same methodology adopted for the jet-cap analysis. As illustrated in Fig. 5 (right), the configuration featuring a counter-swirl chamfer on the long port (corresponding to zero swirl intensity), achieves the highest degree of mixture homogeneity at the TDCf. In this case, σ_{Rel} decreases from 29.2% in the baseline configuration (swirl chamfer on the long port) to slightly above 15%. This improvement arises from the dominance of tumble motion, which governs the in-cylinder flow field. Once the hydrogen jet impacts the piston bowl, it is redirected upward toward the injector region rather than being trapped by the swirl or deflected toward the liner. Consequently, at TDCf the ultra-lean fraction ($\lambda > 3$) drops below 4%, the rich fraction ($\lambda < 1.5$) nearly vanishes ($< 0.03\%$), and about 65% of the charge lies within the optimal λ range ($2.0 < \lambda < 2.6$). Interestingly, the no-chamfer configuration, which generates an intermediate swirl level (approximately 30% lower than the baseline) yields a moderate uniformity ($\sigma_{Rel} = 25.0\%$). In this case, the ultra-lean mixture fraction decreases from 18% (baseline) to below 14%, while the proportion within the optimal λ range increases from 33% to 45%. These findings confirm that, in direct-injection hydrogen engines derived from diesel units with a flat flame deck and side-mounted injector, the swirl motion is the primary mechanism limiting mixing performance.

While global mixing metrics provide an overall assessment, local flow behaviour plays an equally important role in identifying the optimal design. Fig. 6 shows the temporal evolution of λ within the jet cap volume (a) and near the spark plug (b). Inside the cap, λ must remain sufficiently high to prevent the formation of an excessively reactive end-gas region, to mitigate the risk of abnormal combustion phenomena. A clear difference is observed between high- and low-swirl cases. In the zero-swirl configuration (i.e., counter-swirl chamfer on the long port), λ remains close to or slightly above unity from −90 CAD aTDCf to TDCf. This trend results from the dominance of tumble motion, which drives mixture rotation within a plane nearly aligned with the injector. Consequently, the hydrogen jet is continuously entrained inside the cap volume throughout compression. Only in the final stage, as hydrogen disperses across the chamber, λ slightly rises due to leaner charge entering the cap. Conversely, in high-swirl configurations, the jet deviates from the symmetry plane, causing the mixture to rotate on a tilted path. This results in a leaner region below the injector, thus improving scavenging efficiency. At the spark-plug location, λ should remain moderately low and stable over time to ensure combustion stability. In low-swirl conditions, the strong tumble effectively transports hydrogen toward the spark plug, maintaining $\lambda \approx 2$ from −90 CAD aTDCf to TDCf. In the baseline high-swirl case, tumble initially carries hydrogen toward the ignition zone (−90 CAD aTDCf), but the subsequent swirl dominance produces strong λ fluctuations until TDCf. The no-chamfer geometry, corresponding to an intermediate swirl level, yields an average λ near 3

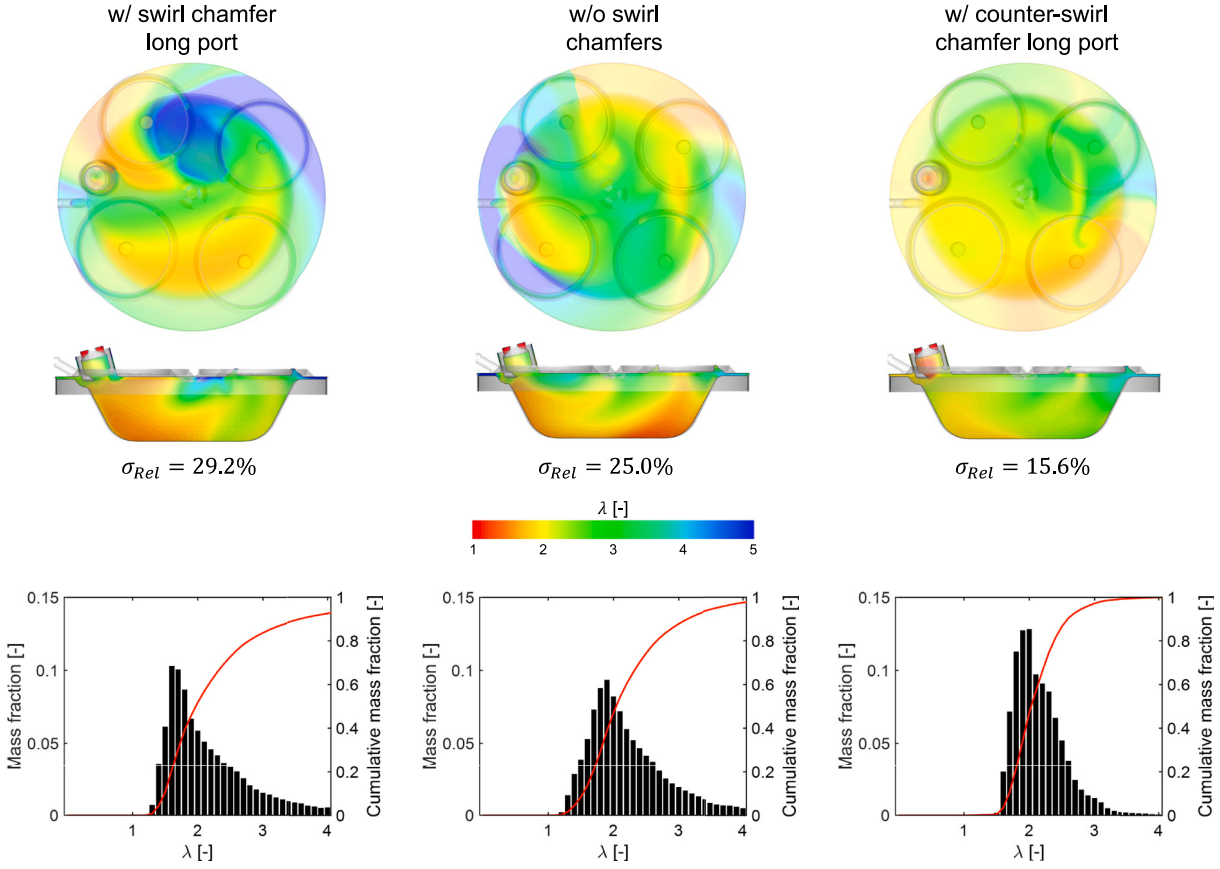


Fig. 5. λ distribution at TDC of combustion (top) and cylinder mass distribution on a λ basis (bottom) for the configurations with swirl chamfer on the long port (left), without swirl chamfers (middle), and with a counter-swirl chamfer on the long port (right).

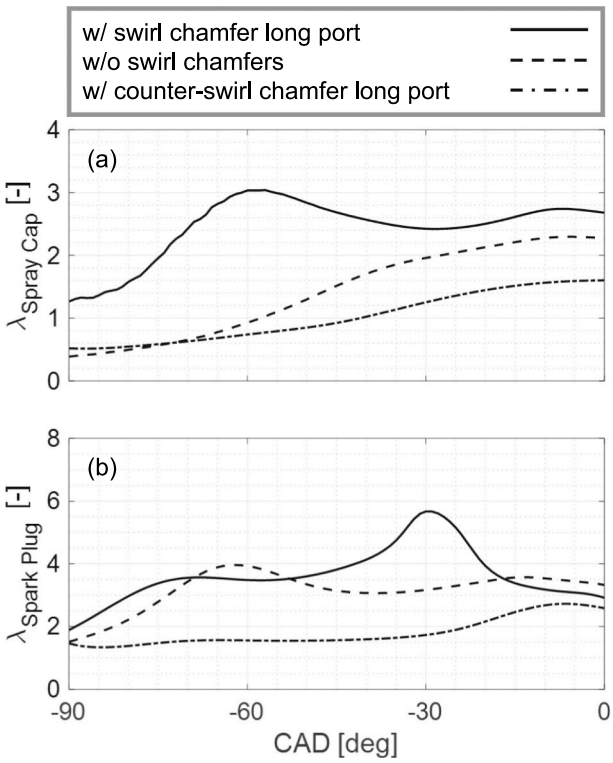


Fig. 6. Mass-weighted average λ in the volume below the injector tip (a), and in the spark plug (b) as a function of the crank angle for the configurations with swirl chamfer on the long port, without swirl chamfers, and with a counter-swirl chamfer on the long port.

between −40 CAD aTDCf and TDCf.

Considering both global and local indicators, the configuration without swirl chamfer was identified as the most effective and therefore selected for engine prototyping and experimental validation. Indeed, this layout offers the best trade-off between overall mixture uniformity (σ_{Rel} = 25.0% at the TDCf) and local mixture features, such as the evolution of λ within the jet cap and in the spark plug region.

4. Testing

The key findings from the simulation campaign were employed to develop the engine demonstrator used for the experimental tests. The prototype was equipped with a new camshaft and a variable nozzle turbine (VNT) boosting system, both defined based on the analyses carried out within the 1D-CFD framework. The combustion chamber geometry, including the injector jet cap, piston bowl shape, and intake valve seat eccentricity, was designed consistently with the outcomes of the 3D-CFD investigations on injection and mixture formation.

4.1. Experimental setup

Experimental activities were performed using the test bench setup schematically represented in Fig. 7.

To complement the schematic layout, a photograph of the actual experimental engine installation is provided in Fig. 8.

In-cylinder pressure was monitored through four Kistler 6056 A piezoelectric transducers, one per cylinder, each featuring a measuring range from 0 to 250 bar and an accuracy of 0.5% of the full scale (FS), as summarized in Table 3. For every analysed operating condition, 200 consecutive engine cycles were recorded for each cylinder with an angular resolution of 0.1 CAD. The maximum permissible peak firing pressure (PFP) was fixed at 150 bar. Whenever this limit was reached or exceeded, an automatic engine shutdown was triggered to ensure safe

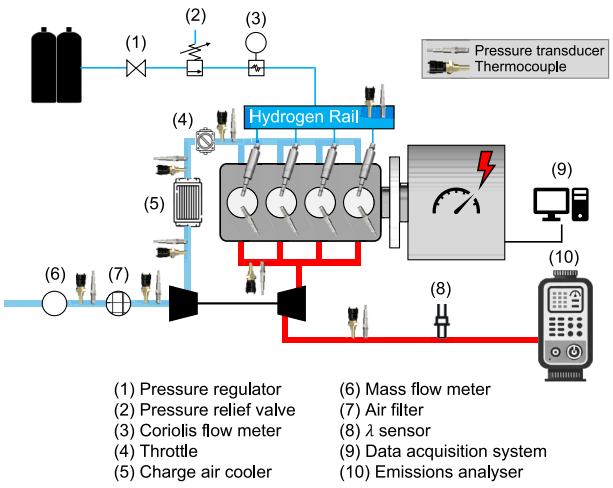


Fig. 7. Layout of the setup and instrumentation used for the experimental testing.

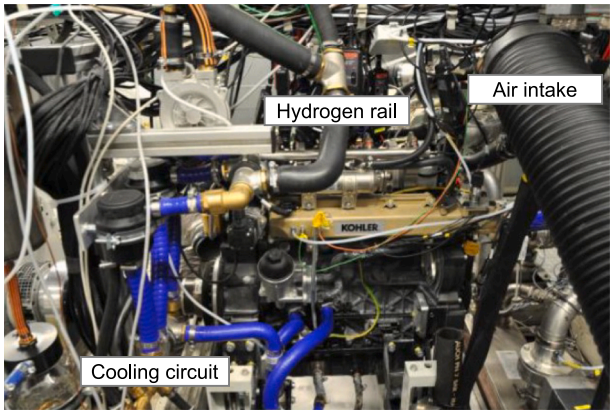


Fig. 8. Experimental test bench setup for the testing of the H_2-ICE prototype.

Table 3
Instrumentation type and accuracy of the equipment used for the experimental testing.

Variable	Instrument	Accuracy
Cylinder pressure	Kistler 6056 A	0.5% FS
Air flow rate	FEV-AirRate	1.0% FS
Pressure (intake line)	Keller M5HB	0.1% FS
Pressure (exhaust line)	Keller M8coolHB	0.1% FS
Hydrogen mass flow meter	Emerson CMFS015M	0.25% FS
Engine torque	HBM T12	0.01% FS
Exhaust gas emissions	FEV EmissionRate FEVER	1.0% FS

operation. The indicated pressure signals were processed using the FEVIS indication system. Low-frequency pressure and temperature data were collected at several locations along the intake system: upstream and downstream of the air filter, at the compressor outlet, downstream of the charge air cooler, and after the throttle body. The pressures at these five measurement points were acquired using Keller M5HB transducers, characterized by a 0–3 bar range and 0.1% FS accuracy. In the exhaust system, low-frequency pressure and temperature were monitored both upstream and downstream of the turbine. A Keller M8coolHB pressure sensor, featuring the same accuracy and range as the M5HB but rated for gas temperatures up to 1000 K, was employed for this purpose. The emission analysis was carried out using the FEV EmissionRate FEVER system, which enabled the real-time measurement

of CO, CO_2, O_2, NO_x, and unburned hydrocarbons. Engine torque was measured via an HBM T12 dynamometer, offering a maximum capacity of 500 Nm and a rotational speed limit of 10,000 rpm. Hydrogen was supplied from high-pressure storage tanks (210 bar, 99.999% purity). The test bench pressure regulator reduced the pressure to 50 bar, which was then further lowered by the hydrogen rail regulator to the injector operating pressure (ranging from 5 to 30 bar). Hydrogen mass flow rate was determined using an Emerson CMFS015M Coriolis mass flow meter positioned upstream of the rail, providing an accuracy of 0.25% FS. The air mass flow rate was measured using an FEV-AirRate flow meter located before the air filter. Instantaneous air and hydrogen flow data were employed to calculate the actual relative air-to-fuel ratio (λ). To validate the computed λ values, an additional lambda sensor was installed in the exhaust line. Both injection and ignition events were managed via a rapid proto-INCA control module. Engine coolant was maintained at a constant temperature of 90 °C, whereas the oil temperature was left unregulated. Hydrogen concentration inside the crankcase was continuously monitored to ensure it remained below 2%, thereby providing a safety margin relative to the lower flammability limit (3.8%) and to assess the efficiency of the crankcase ventilation system. Two experimental configurations were considered: one including an exhaust throttling valve to replicate backpressure levels typical of an exhaust aftertreatment system (EATS), and another employing an actual selective catalytic reduction (SCR) device to achieve near-zero tailpipe NO_x emissions.

The testing campaign initially involved steady-state experiments, in which key calibration parameters, such as relative air-to-fuel ratio, injection timing, and combustion phasing (MFB50), were systematically varied. Subsequently, the optimized engine calibration map was used to assess transient performance and emissions under the NRTC.

4.2. Engine control and limitations

Thanks to hydrogen's high flame speed across a broad λ range and its wide flammability limits [73], H_2-ICEs typically operate under lean conditions. Lean operation enhances thermal efficiency by lowering combustion temperatures, reducing wall heat losses, increasing the specific heat ratio, and minimizing pumping losses through reduced throttling, particularly at low loads. Lower combustion temperatures also mitigate the occurrence of abnormal combustion phenomena and limit NO_x formation. However, lean operation introduces challenges for component design, especially for the charging system, and affects engine operation.

Fig. 9 identifies four regions in the engine map where different constraints limit the maximum achievable λ:

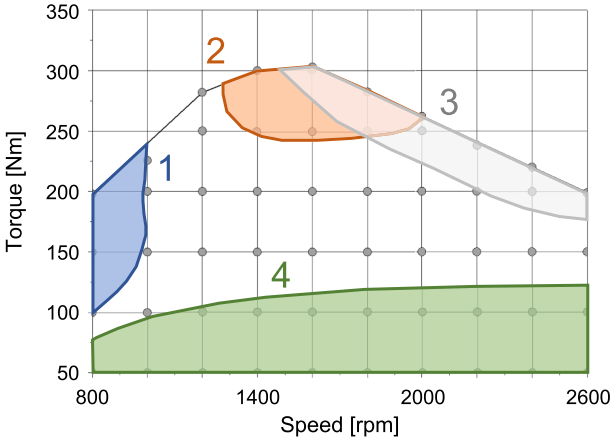


Fig. 9. Engine map with highlighted regions illustrating the operational constraints that limit the maximum achievable λ.

1. Region 1 – Low-speed, high-load: λ is limited by compressor surge, which also increases NO_x formation. As engine speed rises, higher air mass flow allows the compressor to operate further from surge, enabling full-load operation at higher λ.
2. Region 2 – Medium-speed, high-load: λ is mainly limited by abnormal combustion. Indeed, increased air demand at higher load raises intake charge temperature, while higher in-cylinder pressures enhance end-gas autoignition.
3. Region 3 – Medium-to-high-speed, high-load: turbine speed approaches its maximum, limiting λ.
4. Region 4 – Low-load: λ is limited by combustion stability.

Based on this characterization, the H_2-ICE was experimentally calibrated across the entire map using steady-state measurements. Calibration considered charging strategies (i.e., air-to-fuel ratios), injection timing, and ignition timing. To provide representative insight into the engine, three specific conditions were selected for detailed analysis. Two of them correspond to the regions limited by charging performance and combustion stability, respectively, while the third represents a typical mid-load operating point, highly relevant for off-road applications:

- Low-load combustion stability analysis.
- 1000 rpm - 200 Nm (10.1 bar BMEP): the limited air mass flow forces the compressor near surge, restricting λ and strongly influencing efficiency.
- 1800 rpm - 200 Nm (10.1 bar BMEP): the higher mass flow rate enables achieving the same load at higher λ, enabling the assessment of engine behaviour at medium loads under leaner conditions.

4.2.1. Combustion stability at low loads

Operating under high dilution conditions, particularly at low loads, improves engine efficiency by reducing throttling and pumping losses. However, lower intake manifold pressure decreases turbulence intensity, leading to higher combustion variability. These effects are amplified at higher engine speeds, where unstable flow fields coupled with highly stratified mixtures exacerbate variability. Fig. 10 reports coefficient of variation (COV) and lowest normalized value (LNV) of IMEP for three speed regimes (1000, 1800, and 2400 rpm) at 50 Nm (2.5 bar BMEP) across three dilution levels ($\lambda = 1.8$, $\lambda = 2.5$, and $\lambda = 3.0$), considering a MFB50 sweep. The LNV of IMEP represents the minimum IMEP value observed over 800 consecutive engine cycles, normalized with respect to the mean IMEP. Thresholds were set at $COV_{IMEP} = 2.5\%$ and $LNV_{IMEP} = 89\%$ [37] (solid and dashed red lines in Fig. 10, respectively). At 1000 rpm, COV_{IMEP} remains below 2.5% even for highly delayed combustion at $\lambda = 3.0$. At 1800 rpm, the leanest mixture exceeds the COV_{IMEP} limit for MFB50 > 12 CAD aTDCf, while partial misfires occur at more advanced phasing ($LNV_{IMEP} < 90\%$). A similar trend is observed at 2400 rpm. However, in this case, the COV_{IMEP} threshold is exceeded even at $\lambda = 2.5$ for late combustion processes. To maintain stability under lean conditions, MFB50 must remain below 10 CAD aTDCf. This increase in combustion variability with engine speed, at constant MFB50, is primarily attributed to the reduced mixing time, which produces less homogeneous mixtures and greater stratification at higher speeds, ultimately affecting combustion stability.

4.2.2. Effect of λ and MFB50 at low-end torque

The influence of combustion phasing at low-end torque was assessed for three air-to-fuel ratios (i.e., $\lambda = 1.8$, $\lambda = 2.0$, and $\lambda = 2.3$). Higher λ values were not tested due to compressor surge limitations. The end of injection (EOI) was fixed at −100 CAD aTDCf, while MFB50 was varied between 6 and 18 CAD aTDCf. Fig. 11 presents ITE (a), MFB1090 (b), engine-out NO_x (c) emissions, hydrogen slip, and COV_{IMEP} (d) as functions of MFB50. For $\lambda = 2.0$ and 2.3, the maximum ITE is similar but occurs at different combustion phasings. In the leanest case ($\lambda = 2.3$), the

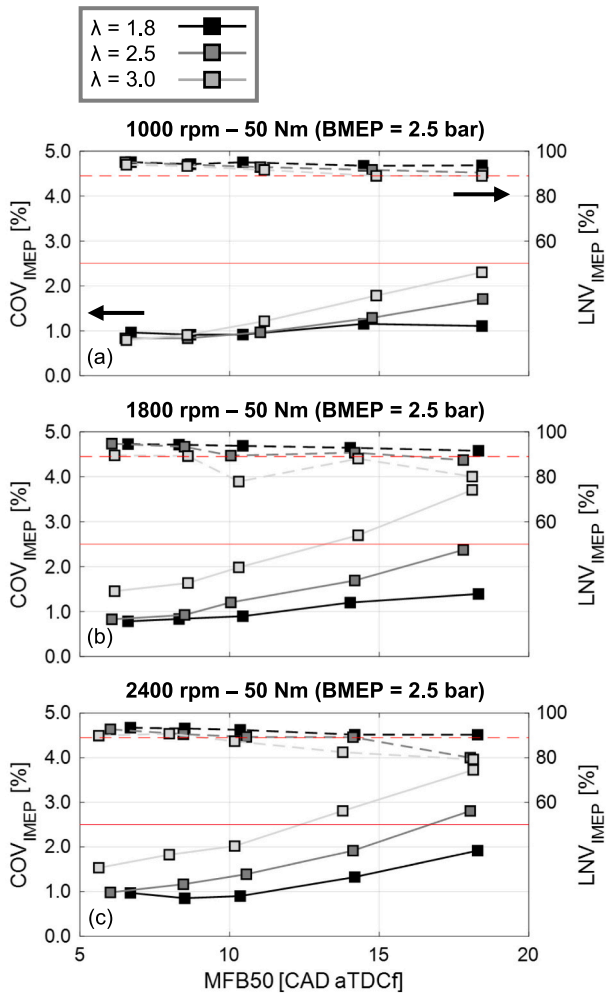


Fig. 10. Coefficient of variation and lowest normalized value of IMEP at 1000 (a), 1800 (b), and 2400 rpm (c) at a constant load of 50 Nm (2.5 bar of BMEP) considering λ = 1.8, λ = 2.5, and λ = 3.0.

optimal MFB50 is advanced (~ 6.5 CAD aTDCf), whereas for λ = 2.0, peak efficiency occurs at MFB50 ~ 8.5 CAD aTDCf. Beyond this difference, ITE remains nearly constant as the efficiency gain at λ = 2.3 from lower wall heat losses is compensated at λ = 2.0 by shorter combustion duration and lower pumping losses. Delaying combustion reduces ITE at all dilution levels due to prolonged burn times, but the associated increase in turbine inlet temperature (~30–40 K from advanced to delayed MFB50) reduces pumping work and partially offsets efficiency losses. Combustion variability grows with λ and retarded phasing due to lower turbulence and temperature, yet remains below 2% even in the most extreme case (λ = 2.3 and delayed MFB50). NO_x emissions are lowest for higher λ and delayed combustion, as both lower in-cylinder temperatures. Compared to the optimal MFB50, delaying combustion reduces NO_x by 70%, 80%, and 85% for λ = 1.8, 2.0, and 2.3, respectively. At the same time, ITE decreases by an average of 1.5%, too. When operating at the optimal MFB50, leaner mixtures achieve substantial NO_x reductions: 70% at λ = 2.0 and 95% at λ = 2.3 versus λ = 1.8. These results indicate that increasing λ is more effective than delaying combustion for reducing NO_x without compromising efficiency. However, At low-end torque, the high backpressure needed to reach the target λ largely offsets the benefits of ultra-lean operation.

4.2.3. *Effect of λ and injection phasing at medium loads*

The effect of injection timing on combustion performance was assessed through an EOI sweep for two air-to-fuel ratios (λ = 2.0 and λ = 2.5) at 1800 rpm and 200 Nm (BMEP = 10.1 bar). The end of injection was varied between −160 and − 80 CAD aTDCf, while MFB50 was kept constant at 8.5 CAD aTDCf. As illustrated in Fig. 12, advancing the injection timing reduces ITE, mainly because delaying injection lowers compression work without compromising combustion. Indeed, combustion duration remains almost constant across the EOI range, with a slight shortening for the latest injection, particularly at the leanest mixture (λ = 2.5). At the same time, NO_x emissions, hydrogen slip, and combustion variability show negligible sensitivity to injection timing. These results indicate that the engine tolerates delayed injections, which can improve efficiency while shortening the residence time of hydrogen in the cylinder prior to ignition, thereby reducing the risk of pre-ignition.

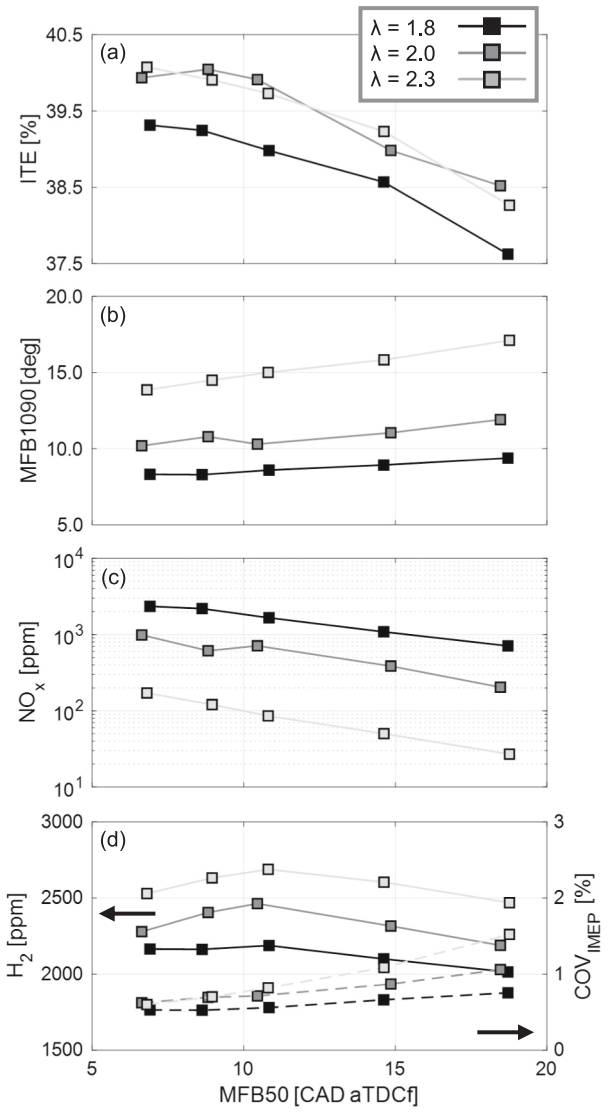


Fig. 11. ITE (a), MFB1090 (b), engine-out NO_x emissions (c), unburned hydrogen and COV_{IMEP} (d) at 1000 rpm - 200 Nm (10.1 bar of BMEP), considering EOI = −100 CAD aTDCf and a MFB50 sweep for λ = 1.8, λ = 2.0, and λ = 2.3.

4.3. *Engine map calibration*

The sensitivity analysis of the main engine control parameters at steady-state WPs, provided the basis for the calibration strategy adopted for the complete engine map. During the initial development stage, experimental activities were carried out without any EATS, with the

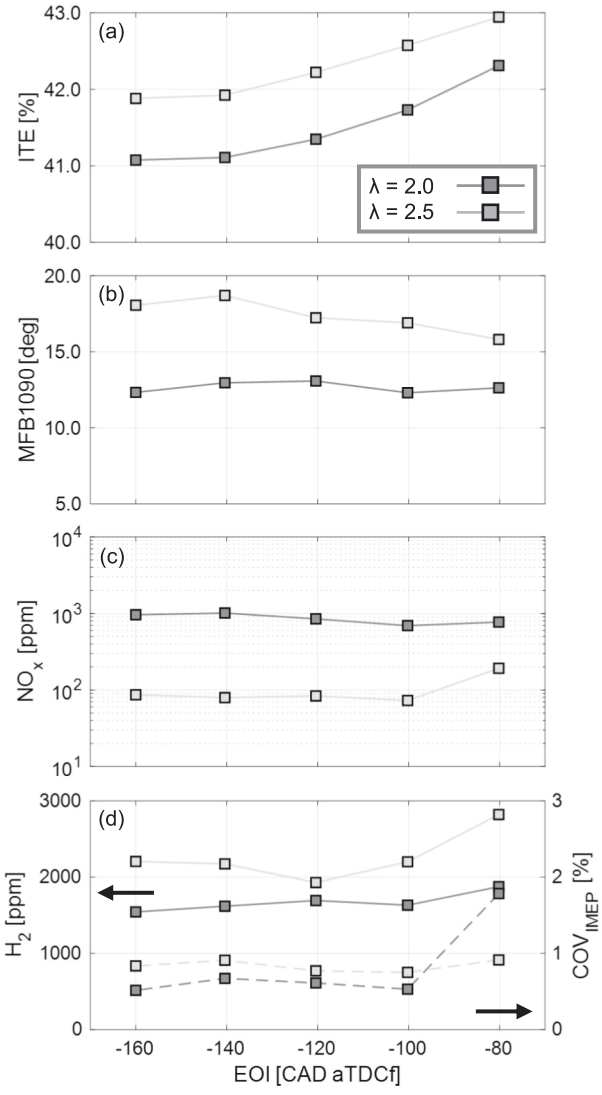


Fig. 12. ITE (a), MFB1090 (b), engine-out NO_x emissions (c), unburned hydrogen and COV_{IMEP} (d) at 1800 rpm - 200 Nm (10.1 bar of BMEP), considering MFB50 = 8 CAD aTDCf and an EOI sweep for λ = 2.0, and λ = 2.5.

objective of evaluating whether the hydrogen-fuelled engine could match the performance of the reference diesel unit. As previously reported by the authors in [74], the engine fulfilled the target load requirements over the entire full-load curve, reaching a maximum torque of 305 Nm at 1600 rpm and sustaining a constant power output of 55 kW between 1800 and 2600 rpm.

In a subsequent phase, the engine calibration was performed with the SCR system installed in the exhaust line, consistently with the configuration adopted for homologation testing. This approach was required to address the dual objective of meeting Stage V engine-out NOx limits over the certification cycle and achieving near-zero tailpipe NOx emissions when the complete EATS is considered. The inclusion of the SCR system during the mapping process also allowed the influence of the associated exhaust backpressure on engine performance to be quantified. Fig. 13 summarizes ITE (a), λ (b), combustion phasing expressed as MFB50 (c), and engine-out NO_x emissions (d) over the full operating map. Leveraging the engine's capability to tolerate relatively delayed injection timing, the calibration was developed using a fixed end of injection set at −80 CAD aTDCf. The additional backpressure introduced by the SCR results in a moderate reduction of the maximum attainable torque at engine speeds above 1200 rpm. Nevertheless, a peak torque of 300 Nm is still achieved between 1400 and 1600 rpm, corresponding to a

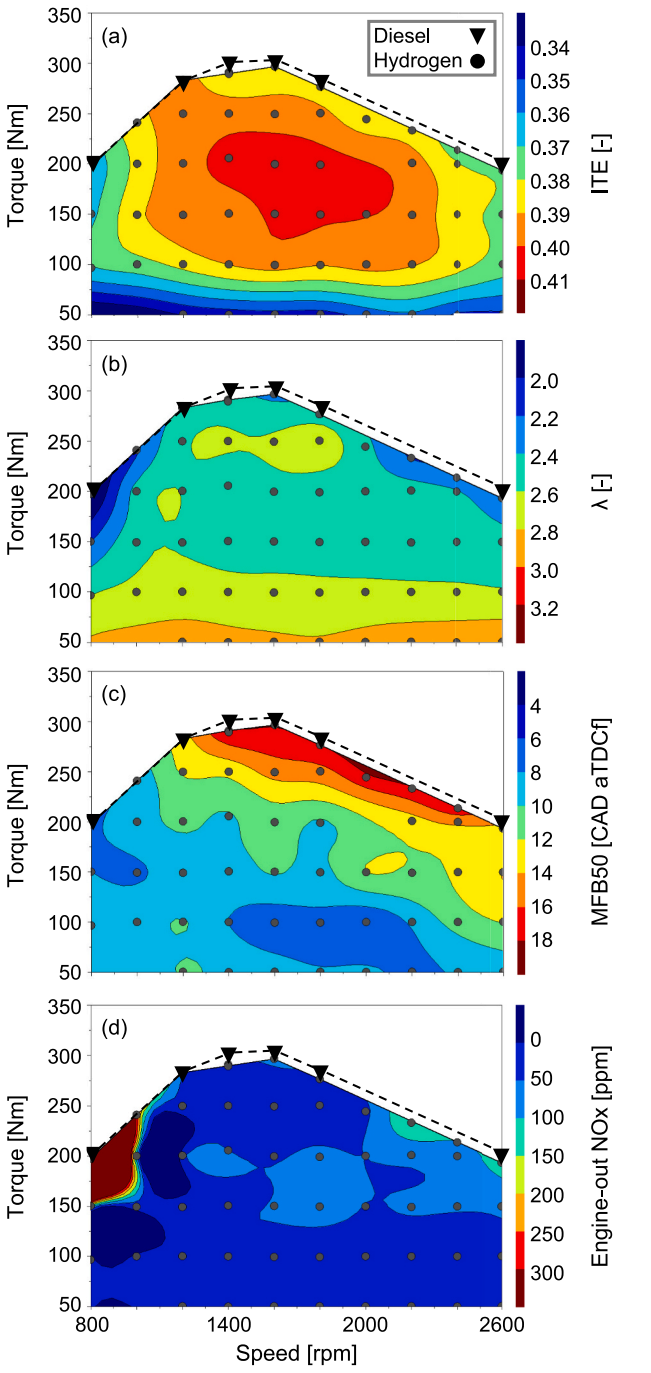


Fig. 13. ITE (a), λ (b), MFB50 (c), and engine-out NO_x emissions (d) throughout the optimized engine map developed including the SCR in the exhaust line.

derating below 5% with respect to the baseline diesel engine. Despite the presence of the exhaust aftertreatment system, high efficiency levels are preserved over a broad range of operating conditions, with ITE values exceeding 40% and a maximum of 40.3% recorded at 1600 rpm and 200 Nm. The engine operates under lean-burn conditions across the entire map. At low loads, highly diluted mixtures (λ > 2.6) are employed without adversely affecting combustion stability, while increasing load levels require a progressive reduction in dilution. The minimum air–fuel ratio, equal to λ = 1.85, is observed in the low-speed high-load region (800 rpm – 200 Nm), where compressor surge limits prevent operation at higher dilution levels, leading to engine-out NO_x emissions above

1000 ppm. Another region characterized by slightly higher NO_x emissions is identified along the full-load curve at engine speeds exceeding 1800 rpm. This behaviour is mainly associated with the reduction of λ toward values around 2.2 due to turbocharger speed constraints, combined with increased intake air temperatures resulting from higher mass flow rates through the charge air cooler. To mitigate NO_x formation under these conditions, combustion phasing was progressively retarded by approximately 10–15 CAD relative to the efficiency-optimal setting. As a consequence, NO_x emissions remain low over most of the operating map, with the low-speed torque region representing the dominant contribution to the overall emission level.

4.4. NO_x emissions on NRTC homologation cycle

After the complete calibration of the main operating parameters across the full engine map, the engine-out NO_x emissions were assessed over the LSI-NRTC. This homologation cycle, specifically designed for large spark-ignition engines (rated power between 19 and 56 kW) employed in off-road applications, aims at reproducing the broad range of speed and load conditions typically encountered in real operation. In the LSI-NRTC, both torque and speed are normalized with respect to the engine's maximum values. This normalization makes the cycle applicable to engines with different power levels, enabling consistent performance and emission comparisons without the need for engine-specific test procedures.

Fig. 14a-b presents the speed and load profiles of the LSI-NRTC applied to the tested engine. The complete test lasts approximately 1200 s (equivalent to 20 min). The first part of the cycle (0–900 s) is characterized by pronounced transient events and large load fluctuations, simulating dynamic working conditions such as those experienced by telehandlers, skid-steer loaders, or agricultural machines during heavy-duty tasks like lifting or towing. These transients are particularly demanding for hydrogen-fuelled engines, as rapid load variations often require temporary mixture enrichment to enhance dynamic response, which in turn leads to increases in engine-out NO_x emissions. In contrast, the final phase of the cycle (900–1200 s) corresponds to high-speed, low-load operation, representative of light-duty tasks or vehicle repositioning. In this regime, the engine runs at nearly constant load and elevated speeds.

In Fig. 14c-d the instantaneous λ together with engine-out and tailpipe NO_x emissions are presented. The experimental campaign was carried out with a SCR system installed in the exhaust line to evaluate its effectiveness under transient conditions. Throughout the cycle, the rapid load variations require frequent and abrupt mixture enrichments to ensure adequate torque response and maintain combustion stability. These transient enrichments produce short, localized peaks in engine-out NO_x emissions, clearly visible in the first 900 s of the test, where load changes are most pronounced. Conversely, during the final segment of the cycle (from roughly 900 to 1200 s), the engine operates under quasi-steady conditions, characterized by high speed and low load. In this phase, the calibration reported in Fig. 13 is applied, resulting in operation with ultra-lean mixtures (average $\lambda \sim 3$). Under these conditions, NO_x formation is almost completely suppressed, and both engine-out and tailpipe emissions approach zero. This confirms that at high-speed/low-load regimes, lean-burn combustion enables near-zero-emission performance without compromising engine stability.

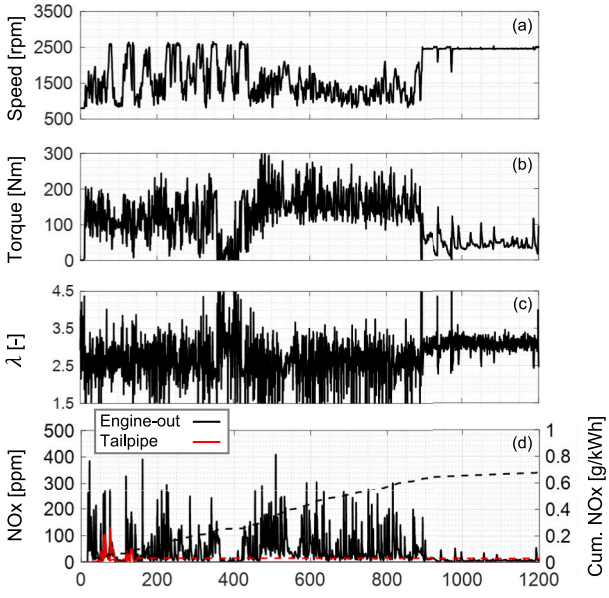


Fig. 14. LSI-NRTC speed (a) and torque (b) profiles, operating λ (c), and engine-out and tailpipe instantaneous and cumulative NO_x emissions (d).

Table 4
Engine-out and tailpipe cumulative NO_x emissions over the LSI NRTC cycle.

LSI NRTC	
Engine-out [g/kWh]	0.68
Tailpipe NO_x [g/kWh]	0.03

As reported in Table 4, the cumulative engine-out NO_x emissions amount to 0.68 g/kWh, remaining well below both the EU Stage V regulatory threshold (4.70 g/kWh for NO_x + non-methane hydrocarbons) and the EPA Tier 5 proposal (2.50 g/kWh for NO_x), thus allowing the engine to operate without a dedicated EATS.

The tailpipe NO_x emissions are over one order of magnitude lower than the corresponding engine-out values, reaching 0.03 g/kWh, and exhibit an interesting temporal trend. Contrary to what might be expected, NO_x levels at the tailpipe are initially zero, then show intermittent peaks, before returning to and remaining at zero for the remainder of the cycle. This behaviour can be attributed to the engine preconditioning procedure. Prior to starting the test, the engine is warmed up to a coolant temperature of 90 °C, bringing the SCR catalyst closer to its effective operating temperature range. As a result, NO_x produced during early combustion phases is fully converted. However, the very lean mixtures used during this initial stage tend to lower the SCR temperature, temporarily reducing its effectiveness. In the subsequent high-load phases, the increased exhaust enthalpy promotes SCR reactivation, increasing conversion efficiency and leading to a drastic reduction of tailpipe NO_x throughout the remainder of the cycle.

5. Conclusions

In the present work, an integrated numerical-experimental methodology was applied to develop a 2.4 L four-cylinder DI H_2-ICE for off-road applications starting from a diesel engine, with only minor hardware modifications. The air-fuel mixing process was optimized via 3D-CFD simulations and subsequently validated on a prototype engine under steady-state and transient conditions, including homologation cycle assessment. The main outcomes are summarized as follows:

- 3D-CFD analysis: optimized jet targeting and reduced swirl intensity significantly improved mixture formation, lowering the relative standard deviation of the equivalence ratio (σ_{Rel}) at TDC from values greater than 45% to approximately 15–25%. This resulted in a strong reduction of ultra-lean ($\lambda > 3$) and rich regions ($\lambda < 1.5$), with up to 65% of the charge within the optimal range ($2.0 < \lambda < 2.6$).
- Steady-state testing: preliminary experimental activities carried out without exhaust aftertreatment demonstrated that the engine was capable of matching the full-load performance of the reference diesel engine, reaching 305 Nm and 55 kW. Further calibration showed that lean-burn operation (λ up to

3.0) combined with optimized combustion phasing enables stable combustion ($COV_{IMEP} < 2\%$) even at very low loads (BMEP = 2.5 bar). The effect of injection phasing was also investigated: delayed injection leads to shorter combustion duration and improved thermal efficiency (compression work reduction), while showing negligible sensitivity in terms of NO_x emissions, hydrogen slip, and combustion stability.

- Effect of SCR integration: the SCR system induced a limited torque derating (<5%, ~5 Nm) due to increased exhaust backpressure. Nevertheless, high efficiency levels (ITE > 40%) were preserved.
- Homologation cycle: over the homologation cycle, the engine achieved engine-out NO_x emissions equal to 0.68 g/kWh, well below EU Stage V (4.70 g/kWh) and EPA Tier 5 (2.50 g/kWh) limits. With the SCR system, tailpipe NO_x emissions were reduced to 0.03 g/kWh, approaching near-zero levels.

The results demonstrate that DI H_2-ICEs can be derived from existing diesel platforms with minimal modifications, achieving diesel-like performance, > 40% ITE, and ultra-low NO_x emissions, thus providing a cost-effective and scalable pathway toward zero-CO_2 powertrains.

CRediT authorship contribution statement

Andrea Scalambro: Software, Methodology, Investigation, Formal analysis, Writing – original draft. **Andrea Piano:** Visualization, Supervision, Writing – review & editing. **Federico Millo:** Resources, Funding acquisition. **Nicola Scinicariello:** Project administration, Conceptualization, Writing – review & editing. **Wladimir Lodi:** Project administration, Conceptualization. **Fabio Mallamo:** Funding acquisition, Conceptualization. **Rosario Loiodice:** Resources, Project administration. **Bartosch Jagodzinski:** Methodology, Data curation. **Avnish Dhongde:** Methodology, Data curation, Writing – review & editing.

Declaration of competing interest

The authors declare that they have no known competing financial interests or personal relationships that could have appeared to influence the work reported in this paper.

Data availability

The data that has been used is confidential.

References

[1] V. Masson-Delmotte, P. Zhai, H.O. Pörtner, D. Roberts, J. Skea, P.R. Shukla, Global Warming of 1.5° C: IPCC Special Report on Impacts of Global Warming of 1.5° C above Pre-Industrial Levels in Context of Strengthening Response to Climate Change, Sustainable Development, and Efforts to Eradicate Poverty, Cambridge University Press, 2022, https://doi.org/10.1017/9781009157940.

[2] Sixth Assessment Report (AR6) of the Intergovernmental Panel on Climate Change (IPCC), Panmao Zhai, 2026.

[3] https://climate.nasa.gov/.

[4] IEA - International Energy Agency. https://www.iea.org/reports/co2-emissions-in-2023, 2023.

[5] European Commission, The European Green Deal, Brussels, 2019.

[6] European Commission, 'Fit for 55': delivering the EU's 2030 climate target on the way to climate neutrality, 2021.

[7] P. Aguilar, B. Groß, Battery electric vehicles and fuel cell electric vehicles, an analysis of alternative powertrains as a mean to decarbonise the transport sector, Sustain. Energy Techn. and Assess. 53 (2022), https://doi.org/10.1016/j.seta.2022.102624.

[8] H. Rösler, B. Van der Zwaan, I. Keppo, J. Bruggink, Electricity versus hydrogen for passenger cars under stringent climate change control, Sustain. Energy Techn. and Assess. 5 (2014) 106–118, https://doi.org/10.1016/j.seta.2013.11.006.

[9] F. Mohammadi, M. Saif, A comprehensive overview of electric vehicle batteries market, E-Prime Adv. Electr. Eng. Electron. Energy 3 (2023), https://doi.org/10.1016/j.prime.2023.100127.

[10] P.K. Senecal, F. Leach, Diversity in transportation: why a mix of propulsion technologies is the way forward for the future fleet, Results Eng. 4 (2019), https://doi.org/10.1016/j.rineng.2019.100060.

[11] O. Coureau, B. Dauverchain, J.-B. Leroy, G. Aufranc, B. Corbières, B. Griffaton, N. Perrot, X. Gautrot, R. Grizivatz, HyMot: H2 engine optimized for light commercial vehicle applications with near-zero emissions, in: 45th International Vienna Motor Symposium, 2024, https://doi.org/10.62626/oi7t-gg3f. ISBN 9783950496932.

[12] C. Cunanan, M.K. Tran, Y. Lee, S. Kwok, V. Leung, M. Fowler, A review of heavy-duty vehicle powertrain technologies: diesel engine vehicles, battery electric vehicles, and hydrogen fuel cell electric vehicles, Clean Technol. 3 (2) (2021) 474–489, https://doi.org/10.3390/cleantechnol3020028.

[13] Z. Abdin, A. Zafaranloo, A. Rafiee, W. Mérida, W. Lipiński, K.R. Khalilpour, Hydrogen as an energy vector, Renew. Sust. Energ. Rev. 120 (2020), https://doi.org/10.1016/j.rser.2019.109620.

[14] S.E. Hosseini, B. Butler, An overview of development and challenges in hydrogen powered vehicles, Int. J. Green Energy 17 (1) (2020) 13–37, https://doi.org/10.1080/15435075.2019.1685999.

[15] Q. Chen, G. Zhang, X. Zhang, C. Sun, K. Jiao, Y. Wang, Thermal management of polymer electrolyte membrane fuel cells: a review of cooling methods, material properties, and durability, Appl. Energy 286 (2021), https://doi.org/10.1016/j.apenergy.2021.116496.

[16] S. Zhang, X. Jin, S. Duan, Z. Yang, T. Xu, H. Zhou, Z. Wang, Hydrogen energy industry and Dongfeng hydrogen internal combustion engine application development, in: 45th International Vienna Motor Symposium, 2024, https://doi.org/10.62626/zm79-5dir.

[17] C.M. White, R.R. Steeper, A.E. Lutz, The hydrogen-fueled internal combustion engine: a technical review, Int. J. Hydrog. Energy 31 (10) (2006) 1292–1305, https://doi.org/10.1016/j.ijhydene.2005.12.001.

[18] K. Klepatz, H. Rottengruber, S. Zeilinga, D. Koch, W. Prümm, Loss analysis of a direct-injection hydrogen combustion engine, in: SAE Technical Papers, SAE International, 2018, https://doi.org/10.4271/2018-01-1686.

[19] M. Medda, V. Calia, M. Di Sacco, F. Gullino, V. Rossi, N. Silvestri, R. Tonelli, F. Zaffino, Challenges and opportunities in developing a Hydrogen High Specific Power SCE in the roadmap towards zero net GHG, in: 32nd Aachen Colloquium Sustainable Mobility, 2023. ISBN 9783000767586.

[20] P. Grabner, E. Schutting, M. Schneider, Hydrogen ICE: state of the art and future potential for real-world application, in: 32nd Aachen Colloquium Sustainable Mobility, 2023. ISBN 9783000767586.

[21] M. De Feo, C. Chaillou, E. Laigle, G. Lurf, N.J. Kunder, M. Wieser, K. Wilfling, M. Schneider, J. Torkelson, The role of lubricant formulation in controlling pre-ignition phenomena in a H2-ICE, in: 45th International Vienna Motor Symposium, 2024, https://doi.org/10.62626/4r79-bfca.

[22] A. Srna, G. Nyrenstedt, R. Rajasegar, Towards conceptual understanding of pre-ignition mechanisms in hydrogen-fueled engines – recent progress at Sandia National Laboratories, in: 45th International Vienna Motor Symposium, 2024, https://doi.org/10.62626/935j-t4ij.

[23] R. Rajasegar, A. Srna, I. Barbery, R. Novella, On the phenomenology of hot-spot induced pre-ignition in a direct-injection hydrogen-fueled, heavy-duty, optical-engine, in: SAE Technical Papers, SAE International, 2023, https://doi.org/10.4271/2023-32-0169.

[24] P. Grabner, M. Schneider, K. Gschiel, Formation mechanisms and characterization of abnormal combustion phenomena of hydrogen engines, in: SAE Technical Paper (2023–32–0168), 2023, https://doi.org/10.4271/2023-32-0168.

[25] S. Shariff, W. Au, D. Mumford, U. Lundqvist, E. Olofsson, A. Palmkvist, J. Linderyd, M. Pelz, Westport fuel systems' H2 HPDI TM technology applied to the Scania CBE1 Engine, in: 45th International Vienna Motor Symposium, 2024, https://doi.org/10.62626/ogzk-z3ry.

[26] A. Ferrarese, E.A. Kumoto, R. Marquard, M. Wieser, A. Arnberger, U. Lundqvist, D. Mumford, J. Walker, Hydrogen internal combustion engine with highest efficiency, in: 11th International Engine Conference - ATZ, 2024.

[27] B. Geringer, Hydrogen combustion concepts: comparison of port fuel injection with spark ignition and High Pressure Direct Injection (HPDITM) – power density, efficiency, and emissions, in: 44th International Vienna Motor Symposium, 2023. ISBN 9783950496925.

[28] T. Briggs, R. Williams, Zero impact engines: a demonstration of H2-ICE technologies for zero-CO2 and near-zero NOX in the North American Class 8 Heavy-Duty Truck Market, in: 45th International Vienna Motor Symposium, 2024, https://doi.org/10.62626/ws3g-faaf.

[29] C. Ramalho Leite, M. Laignel, P. Brequigny, J. Borée, F. Foucher, Experimental combustion analysis in a gasoline baseline hydrogen-fueled internal combustion engine at Ultra-Lean Conditions, in: SAE Technical Papers, SAE International, 2023, https://doi.org/10.4271/2023-24-0073.

[30] J. Gao, X. Wang, P. Song, G. Tian, C. Ma, Review of the backfire occurrences and control strategies for port hydrogen injection internal combustion engines, Fuel 307 (2022), https://doi.org/10.1016/j.fuel.2021.121553.

[31] V. Kalaskar, G. Conway, G. Handa, S. Joo, D. Williams, Challenges and opportunities with direct-injection hydrogen engines, in: SAE Technical Papers, SAE International, 2023, https://doi.org/10.4271/2023-01-0287.

[32] T. Wallner, A.M. Nande, J. Naber, Evaluation of injector location and nozzle design in a direct-injection hydrogen research engine, in: SAE Technical Papers (2008–01–1785), 2008, https://doi.org/10.4271/2008-01-1785.

[33] M. Mohamed, K. Longo, H. Zhao, J. Hall, A. Harrington, Hydrogen engine insights: a comprehensive experimental examination of port fuel injection and direct injection, in: SAE Technical Papers, SAE International, 2024, https://doi.org/10.4271/2024-01-2611.

[34] S. Özdemir, F. Schmitt, C. Rudek, V. Cogo, G. Prante, K. Wittek, The boosting system for an off-road hydrogen internal combustion engine, in: 27th Supercharging Conference, 2023.

[35] L. Jaeger, P. Pribyl, F. Akar, P. Foucek, F. Eckl, P. Davies, F. Paulicelli, S. Kumar, M. Mirzaeian, S. Langridge, Divided flow VNT for heavy duty engines, in: 27th Supercharging Conference, 2023.
[36] J. Kim, S. Rajoo, A numerical study on turbocharging system for PFI-SI type hydrogen combustion engine, in: SAE Technical Papers, SAE International, 2021, https://doi.org/10.4271/2021-24-0094.
[37] M. Bunce, B. Seba, R. Andreutti, Z. Yan, N. Peters, Development of a high power, low emissions heavy duty hydrogen engine, in: SAE Technical Papers, SAE International, 2024, https://doi.org/10.4271/2024-01-2610.
[38] J. Achenbach, B. Jagodzinski, A. Schloßhauer, M. Stadermann, L. Virnich, Boosting concepts for hydrogen combustion engines for different vehicle applications, in: 27th Supercharging Conference, 2023.
[39] K. Gschiel, S. Roiser, M. Schneider, K. Wilfling, H. Eichlseder, Measures to improve the transient behaviour of hydrogen ICE, in: 27th Supercharging Conference, 2023.
[40] A. Kufferath, D. Naber, S. Bareiss, G. Cornetti, M. Krüger, H. Rösch, The synergy between operating strategy, hydrogen injection system and exhaust-gas aftertreatment as the key to an attractive hydrogen engine concept, in: 45th International Vienna Motor Symposium, 2024, https://doi.org/10.62626/4a8f-bnpk.
[41] S. Tafel, L. Martin, Bosch engineering high-performance H2 engine demonstrator, in: 45th International Vienna Motor Symposium, 2024, https://doi.org/10.62626/9xw5-fgij.
[42] H. Huang, K. Xing, H. Lu, Y. Wang, Z. Tu, Y. Qin, T. Lin, H. Huang, Study on the potential of injection strategies to suppress knock combustion in direct-injection hydrogen engines under high compression ratio, Fuel 417 (2026), https://doi.org/10.1016/j.fuel.2026.138632.
[43] N. Shimmura, M. Oikawa, S. Yamada, Y. Mihara, Y. Takagi, Experimental and numerical investigation of high-flow-rate injection focusing on improved thermal efficiency and output performance in low-pressure direct-injection hydrogen engines, J. Energy Inst. 125 (2026) 102463, https://doi.org/10.1016/j.joei.2026.102463.
[44] F.S. Mortellaro, N. Silvestri, F. Zaffino, M. Medda, M. D'Elia, V. Viswanathan, R. Rothbauer, Effect of start of injection in a hydrogen-fueled disi engine: experimental and numerical investigation, in: SAE Technical Papers, SAE International, 2023, https://doi.org/10.4271/2023-24-0015.
[45] T. Durand, P. Adomeit, M. Blomberg, Y. Jeihouni, F. Michelet, L. Combemale, S. Meyer, Combustion chamber development to maximize the performance of the hydrogen combustion engine for the T1 ultimate category of the Dakar Rally Competition, in: SAE International Journal of Advances and Current Practices in Mobility, SAE International, 2023, pp. 2312–2318, https://doi.org/10.4271/2023-01-0737.
[46] A. Mohammadi, M. Shioji, Y. Nakai, W. Ishikura, E. Tabo, Performance and combustion characteristics of a direct injection SI hydrogen engine, Int. J. Hydrog. Energy 32 (2) (2007) 296–304, https://doi.org/10.1016/j.ijhydene.2006.06.005.
[47] Y. Li, W. Gao, P. Zhang, Y. Ye, Z. Wei, Effects study of injection strategies on hydrogen-air formation and performance of hydrogen direct injection internal combustion engine, Int. J. Hydrog. Energy 44 (47) (2019) 26000–26011, https://doi.org/10.1016/j.ijhydene.2019.08.055.
[48] J.N. Geiler, T. Rabe, E. Schünemann, K.M. Springer, M. Blomberg, M. Kirzinger, Light commercial vehicle with a H2 engine hybrid powertrain, in: 32nd Aachen Colloquium Sustainable Mobility, 2023. ISBN 9783000767586.
[49] D.-I. Jan Niklas Geiler, D.-I. Klaus Moritz Springer, D.-I. Thomas Lorenz, M. Sc Michael Blomberg, M. Sc Jens Achenbach, D.-I. Peter Bloch, H2 engine hybrid powertrain for future light commercial vehicles, in: 11th International Engine Conference - ATZ, 2024.
[50] D. Lejsek, D. Seboldt, J. Niklas Geiler, P. Leick, M. Frank, K.G. Stapf, Mixture formation and combustion in a passenger car engine with low pressure H2 direct injection, in: 19th Symposium "Sustainable Mobility, Transport and Power Generation", 2023.
[51] M. Rieß, M. Brauer, J. Maaß, V.L. Römer, Development of Jet Caps for Hydrogen Combustion Processes with Low-pressure Direct Injection, MTZ Worldwide 84 (2023) 26–33, https://doi.org/10.1007/s38313-023-1490-z.
[52] C. Mandanis, R. Vinod Bethi, P. Jochmann, R. Hellmann, F. Köpple, Virtual product development for the hydrogen direct injection engine (H2-DI), in: 11th International Engine Conference - ATZ, 2024.
[53] O. Weber, Dipl-I.J. Leberwurst, N. Jochen Broz, J. Steinmill, Optimized hydrogen injection for lowest NOx emissions, in: 11th International Engine Conference - ATZ, 2024.
[54] Q. Zuo, D. Yang, Z. Shen, C. Kou, Y. Qin, W. Chen, Y. Wang, Z. Wang, Q. Guan, Optimization of direct injection parameters for lean-burn hydrogen-ammonia engines using Kriging surrogate model coupled NSGA-II, Renew. Energy 256 (2026), https://doi.org/10.1016/j.renene.2025.124662.
[55] B. Suatean, G. Cican, S. Guilain, G. De-Paz-Alcolado, Optimization of hydrogen combustion in Diesel engines: a CFD-based approach for efficient hydrogen mixing and emission reduction, Fuels 6 (2) (2025) 27, https://doi.org/10.3390/fuels6020027.
[56] O. Özener, F. Akar, Enhancing hydrogen internal combustion engine efficiency through improvement of injection timing and mixture homogenization dynamics, Int. J. Hydrog. Energy 176 (2025), https://doi.org/10.1016/j.ijhydene.2025.151561.
[57] G. Dober, W. Piock, L. Doradoux, G. Meissonnier, D.G. Mathieu, D. Baralon, A. Laurent, Y. Rimlinger, L. Breton, On the road experience with a LCV H2 ICE: a practical path to eliminate emissions, in: 32nd Aachen Colloquium Sustainable Mobility, 2023. ISBN 978-3-00-076758-6.
[58] L. Rouleau, F. Duffour, B. Walter, R. Kumar, L. Nowak, Experimental and numerical investigation on hydrogen internal combustion engine, in: SAE Technical Papers, SAE International, 2021, https://doi.org/10.4271/2021-24-0060.
[59] R. Rezaei, C. Hayduk, A. Fandakov, M. Rieß, M. Sens, T.O. Delebinski, Numerical and experimental investigations of hydrogen combustion for heavy-duty applications, in: SAE Technical Papers, SAE International, 2021, https://doi.org/10.4271/2021-01-0522.
[60] J. Bieneman, F. Mendes De Araujo, N. Nachappa, I. Kushalappa, Hydrogen internal combustion engine component investigation and development for heavy-duty truck applications, in: *Proceedings of the ASME 2023 ICE Forward Conference. ASME 2023 ICE Forward Conference*, 2023, https://doi.org/10.1115/ICEF2023-110098.
[61] J.L. Beduneau, L. Doradoux, G. Meissonnier, M. Da Graca, Y. Rimlinger, G. Dober, B. Gomot, W.F. Piock, Powertrains for High Intensity Applications – 24 Hours with H2ICE, in: 45th International Vienna Motor Symposium, 2024, https://doi.org/10.62626/wiwh-4y3g.
[62] L. Virnich, A. Dhongde, B. Franzke, R. Tensing, M. Can Kayacan, Tailored cooling and charge motion concept for spark ignited hydrogen combustion engine to achieve highest efficiency and power density, in: 11th International Engine Conference - ATZ, 2024.
[63] G. Maio, A. Boberic, L. Giarracca, D. Aubagnac-Karkar, O. Colin, F. Duffour, K. Deppenkemper, L. Virnich, S. Pischinger, Experimental and numerical investigation of a direct injection spark ignition hydrogen engine for heavy-duty applications, Int. J. Hydrog. Energy 47 (67) (2022) 29069–29084, https://doi.org/10.1016/j.ijhydene.2022.06.184.
[64] R. Scarcelli, T. Wallner, N. Matthias, V. Salazar, S. Kaiser, Numerical and optical evolution of gaseous jets in direct injection hydrogen engines, in: SAE Technical Papers, 2011, https://doi.org/10.4271/2011-01-0675.
[65] R. Scarcelli, T. Wallner, V.M. Salazar, S.A. Kaiser, Modeling and experiments on Mixture Formation in a Hydrogen Direct-Injection Research Engine, SAE Int. J. Engines 2 (2) (2010) 530–541.
[66] R. Heindl, H. Eichlseder, C. Spuller, F. Gerbig, K. Heller, New and innovative combustion systems for the H2-ICE: compression ignition and combined processes, in: SAE Technical Papers, 2009.
[67] A.A. Amsden, A Particle Numerical Model for Wall Film Dynamics in Port-Injected Engines, JSTOR, 1996.
[68] Advanced Simulation Methodologies for Hydrogen Combustion Engines, 2026.
[69] A. Scalambro, Advanced Computational Simulation Methodologies to Enhance Hydrogen Internal Combustion Engine Development, Politecnico di Torino, Torino, 2025.
[70] A. Scalambro, A. Piano, F. Millo, N. Scinicariello, W. Lodi, A. Dhongde, G. Sammito, Numerical analysis of the hydrogen-air mixture formation process in a direct-injection engine for off-road applications, Int. J. Hydrog. Energy 77 (2024) 1286–1295, https://doi.org/10.1016/j.ijhydene.2024.06.193.
[71] M. Ozkara, M.Z. Gul, Optimization of a Heavy-Duty Hydrogen-Fueled Internal Combustion Engine Injector for Optimum Performance and Emission Level, Appl. Sci. (Switz.) 15 (15) (2025), https://doi.org/10.3390/app15158131.
[72] S. Breda, V. Patrizi, F. Berni, R. Tonelli, F.S. Mortellaro, S. Fontanesi, Computational study of injector cap design for optimized mixing and combustion in a high-performance DI hydrogen engine, Int. J. Hydrog. Energy 138 (2025) 129–150, https://doi.org/10.1016/j.ijhydene.2025.05.085.
[73] S. Verhelst, T. Wallner, Hydrogen-fueled internal combustion engines, Prog. Energy Combust. Sci. 35 (6) (2009) 490–527, https://doi.org/10.1016/j.pecs.2009.08.001.
[74] F. Millo, A. Scalambro, A. Piano, F. Mallamo, R. Loiodice, N. Scinicariello, W. Lodi, Development and testing of a hydrogen direct injection internal combustion engine for off-road applications, in: SIA Powertrain 2025, Paris, 2025.